Impact of Device Parameters on Thermal Performance of High-Speed Oxide-Confined 850-nm VCSELs

Prashant P. Baveja, *Student Member, IEEE*, Benjamin Kögel, Petter Westbergh, Johan S. Gustavsson, Åsa Haglund, Drew N. Maywar, *Member, IEEE*, Govind P. Agrawal, *Fellow, IEEE*, and Anders Larsson, *Senior Member, IEEE*

Abstract—We study the impact of device parameters, such as inner-aperture diameter and cavity photon lifetime, on thermal rollover mechanisms in 850-nm, oxide-confined, vertical-cavity surface-emitting lasers (VCSELs) designed for high-speed operation. We perform measurements on four different VCSELs of different designs and use our empirical thermal model for calculating the power dissipated with increasing bias currents through various physical processes such as absorption within the cavity, carrier thermalization, carrier leakage, spontaneous carrier recombination, and Joule heating. When reducing the top mirror reflectivity to reduce internal optical absorption loss we find an increase of power dissipation due to carrier leakage. There is therefore a trade-off between the powers dissipated owing to optical absorption and carrier leakage in the sense that overcompensating for optical absorption enhances carrier leakage (and vice versa). We further find that carrier leakage places the ultimate limit on the thermal performance for this entire class of devices. Our analysis yields useful design optimization strategies for mitigating the impact of carrier leakage and should thereby prove useful for the performance enhancement of 850-nm, high-speed, oxide-confined VCSELs.

Index Terms—Carrier leakage, photon lifetime, thermal effects, vertical cavity surface emitting lasers.

I. INTRODUCTION

850 nm THE standard wavelength for various data communication protocols. Further, commercial multimode fibers and polymer waveguides are optimized for the 850-nm wavelength band [1]. This has fueled the development of high-speed, 850-nm VCSELs with data rates as high as 40 Gb/s

P. P. Baveja and G. P. Agrawal are with the Institute of Optics, University of Rochester, Rochester, NY 14627 USA (e-mail: baveja@optics.rochester.edu).

P. Westbergh, J. S. Gustavsson, B. Kögel, Å. Haglund, and A. Larsson are with the Photonics Laboratory, Department of Microtechnology and Nanoscience, Chalmers University of Technology, SE-412 96 Göteborg, Sweden.

D. N. Maywar is with the Department of Electrical, Computer, and Telecommunications Engineering Technology, Rochester Institute of Technology, Rochester, NY 14623-5603 USA.

Color versions of one or more of the figures in this paper are available online at http://ieeexplore.ieee.org.

Digital Object Identifier 10.1109/JQE.2011.2176554

[2], [3] for diverse applications including high-performance computing, optical interconnects, and consumer electronics [2], [4], [5].

Compared to VCSELs operating in the wavelength range of 980-1100 nm [6], pushing the data rate of 850-nm VCSELs beyond 40 Gb/s has posed several technological challenges and has required considerable development effort [7]–[13]. For example, a high differential gain has required the use of strained quantum wells (QWs) by adding indium to the GaAs material. This causes a red shift of the gain-peak, which in turn has to be compensated by increasing the Al content in the barrier layers and by reducing the QW width [7]. However, a reduced QW width enhances carrier leakage [14], the magnitude of which worsens with increasing device temperatures, thereby limiting the high-speed operation [15].

High-speed operation of VCSELs is achieved by reducing the cavity photon lifetime [8], increasing the differential gain [13], and reducing the gain-compression coefficient by optimizing the separate-confinement heterostructure (SCH) for a short carrier capture time [9]. High speed oxide confined VCSELs commonly employ multiple oxide layers [8] for reducing the oxide capacitance. Pad capacitance is reduced by using low-k dielectric material such as benzocyclobutene (BCB) [10] or polyimide [11], [12]

In the current state-of-the-art 850-nm VCSELs, self-heating effects are the biggest hurdle in improving the modulation bandwidth beyond 23 GHz [3]. Self-heating manifests itself as premature rollover of the optical power with increasing bias current, under continuous-wave (CW) operation. The subsequent saturation of the photon density within the active region limits VCSEL's modulation speed. Traditionally, self-heating effects have been ameliorated by reducing series resistance [10], [13] together with thermal impedance [12], [13]. However, it is equally important to understand the interplay between various power dissipation mechanisms [16], [17] for optimizing the device design for improving the thermal performance.

We recently developed a method for assessing the relative importance of various thermal rollover mechanisms in VCSELs from basic CW measurements and empirical modeling [17]. We applied our method to a specific 850-nm VCSEL, optimized for high-speed operation, and found that in that device power dissipation resulting from linear

mechanisms (optical absorption, carrier thermalization, carrier leakage, and spontaneous carrier recombination) exceeded the quadratic power dissipation resulting from series resistance at all ambient temperatures and bias currents. We further found that the carrier leakage worsened with increasing ambient temperature. In fact, carrier leakage was the most dominant contributor to thermal rollover for that particular device.

In this paper, we compare the thermal performance of four different 850-nm high-speed VCSELs with different designs and show that our model [17] is universally applicable with reasonable accuracy. The aim is to study the impact of device parameters, such as inner-aperture diameter and the cavity photon lifetime, on various thermal rollover mechanisms. In VCSELs where cavity photon lifetime is controlled by the top DBR reflectivity, we find a trade-off between optical absorption and carrier leakage in the sense that overcompensating for one worsens the other. We also demonstrate that increasing inner aperture diameter (leading to a reduction in thermal impedance and series resistance) and reducing photon lifetime both have the same impact of delaying the onset of the rapid increase in carrier leakage, which in turn delays the onset of thermal rollover. Therefore, carrier leakage places the ultimate limit on the thermal performance for this entire class of 850-nm devices. We also discuss useful design-optimization strategies for mitigating carrier leakage. The rest of the paper is organized as follows. In Section 2 we briefly describe key elements of our empirical thermal model. In Section 3 we present the CW measurement results for the four VCSELs with an emphasis on their designs. In Section 4 we present the numerical results and compare them with the measured data. In Section 5 we present a comparative thermal analysis for the four VCSELs and study the impact of device parameters on the thermal performance. Some concluding remarks are preseted in Section 6.

II. EMPIRICAL THERMAL MODEL

The details of our empirical thermal model can be found in [17]. Briefly, our model relates the power dissipated as heat to macroscopic VCSEL parameters. The temperature dependence of these parameters is extracted from a few basic CW measurements. The total power dissipated as heat can be written as

$$P_{tot} = P_{QPD} + P_{LPD} \qquad (1)$$

where P_{QPD}, or quadratic power dissipation, is the power dissipated across the series resistance R_s

$$P_{QPD} = R_s(T_a, I_b)I_b^2 = \frac{dV_b(T_a, I_b)}{dI_b}I_b^2. \qquad (2)$$

Here, I_b is the bias current, T_a is the ambient temperature, and R_s has been replaced by the differential resistance (dV_b/dI_b) at a given bias voltage V_b. We have included a direct dependence of series resistance on current caused by charge accumulation at the hetero-interfaces in the distributed Bragg reflectors (DBRs) as well as power dissipated through voltage drop across the diode [18]; it leads to a reduction in R_s with I_b [17].

P_{LPD}, or linear power dissipation, is the sum total of carrier thermalization, spontaneous carrier recombination, carrier leakage, and internal optical loss. It can be written as

$$P_{LPD} = P_{therm} + P_{rec} + P_{leak} + P_{abs} = K(T)I_b \qquad (3)$$

where P_{therm} is the power dissipation from carrier thermalization, P_{rec} corresponds to spontaneous carrier recombination, P_{leak} corresponds to carrier leakage and P_{abs} corresponds to absorption of stimulated photons in the VCSEL cavity. Below lasing threshold, it is assumed that all spontaneous recombination events produce heat [17]. $K(T)$ is the LPD coefficient whose value also depends on the device temperature T (and as a consequence on both T_a and I_b). Here, $T = T_a + \Delta T$ is the sum of ambient temperature T_a and increase ΔT in the device temperature induced by the bias current. Henceforth, the value of any particular device parameter corresponds to a fixed T_a and I_b (unless specified otherwise).

Above lasing threshold, where self-heating becomes significant, the LPD coefficient $K(T)$ can be expressed in terms of macroscopic VCSEL parameters as [17]

$$K(T) = \frac{1}{q}E_B(T) - \frac{1}{q}E_L(T)\eta_i(T)[1 - \{I_{th}(T)/I_b\}]$$
$$\times \left[1 - \frac{\alpha_i(T) + \alpha_m^B(T)}{\alpha_i(T) + \alpha_m^T(T) + \alpha_m^B(T)}\right] \qquad (4)$$

where $E_B(T)$ and $E_L(T)$ are the temperature-dependent barrier-bandgap energy and laser-photon energy (in eV), respectively, q is the electron charge, $I_{th}(T)$ is the threshold current, $\eta_i(T)$ is the internal quantum efficiency, $\alpha_m^T(T)$ and $\alpha_m^B(T)$ are optical losses through the top and bottom DBR, respectively, and $\alpha_i(T)$ is the internal cavity loss.

The device temperature is obtained using the thermal impedance $R_{th}(T)$ which relates the change in T to the P_{tot} as [13]

$$T = T_a + \Delta T = T_a + R_{th}(T)\left[P_{QPD} + P_{LPD}\right]. \qquad (5)$$

Finally, the optical power emitted through the top DBR is calculated using [18]:

$$P_{opt}(T, I_b) = \frac{\eta_i(T)[I_b - I_{th}(T)]\alpha_m^T(T)}{\alpha_m^T(T) + \alpha_m^B(T) + \alpha_i(T)}\left(\frac{hc}{q\lambda(T)}\right) \qquad (6)$$

where λ is the emission wavelength, c is the speed of light and h is the Planck constant. Equations (1) to (4) are used to calculate P_{tot} as a function of I_b. Equations (5) and (6) then provide variations in T and P_{opt} with I_b, respectively.

The temperature dependence of the macroscopic VCSEL parameters is found as follows: $E_B(T)$ is determined from the Varshini equations [17], [19]; $E_L(T)$ is estimated from temperature dependence of the lasing wavelength $\lambda(T)$ of the fundamental LP_{01} mode as a function of ambient temperature [17]; $I_{th}(T)$, $R_{th}(T)$ and $\eta_i(T)$ are quantified from the measurements of the emitted optical power, voltage and emission wavelength as a function of the I_b over a range (15 to 100 °C) of ambient temperatures [17]. The measurements are performed under CW conditions, and temperature dependence is extracted from data recorded at or just above threshold where self-heating can be assumed to be negligible ($T \approx T_a$).
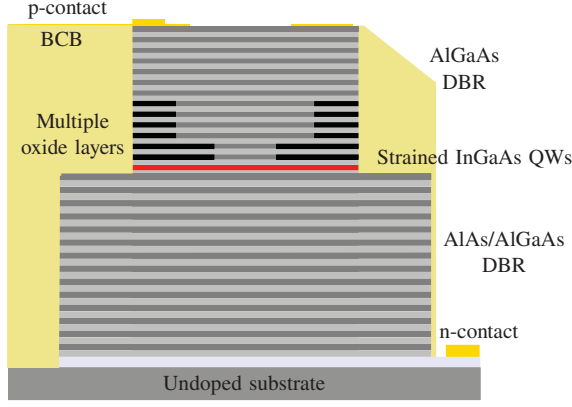
Fig. 1. Schematic of the structure common to all four VCSELs. Benzo-cyclo-butene (BCB) is employed to reduce parasitic capacitance. Six layers are used for forming an oxide aperture (dark shaded region). Other details of the device design can be found in [20].

The measured value of $\Delta\lambda/\Delta T$ for all the device is around 0.06 nm/°C. This quantity is used to estimate the device temperature at various values of T_a and I_b.

The internal loss $\alpha_i(T)$ is extracted from the measured dependence of output power on I_b (just above threshold) for VCSELs with different top-DBR reflectivities. This reflectivity is varied by changing the thickness of the top layer (using dry etching), which controls the phase of the surface reflection. The method is described in [8]. A linear increase in the internal optical loss with temperature for these devices is consistent with a temperature-induced increase of the free-carrier absorption coefficient [8]. Finally, temperature dependence of the transmission loss through the top and bottom DBRs is calculated using an effective index model that takes into account the temperature dependence of the refractive index of the constituent DBR layers [8], [17].

III. CW MEASUREMENTS ON FOUR VCSELs

A. Devices Under Test

The basic structure, common to all four 850-nm VCSELs and shown in Fig. 1, is grown on undoped GaAs substrates. It employs an oxide-confined configuration optimized for high speed modulation [20]. The top and bottom DBRs are fabricated with graded interfaces and modulation doping to reduce their electrical resistance [13]. The bottom DBR is partly composed of AlAs to lower its thermal impedance [8]. The active region is made of five strained InGaAs quantum wells for improved differential gain [7] and is surrounded by a SCH designed for efficient carrier trapping and low gain-compression [9], [20]. As indicated with dark shading in Fig. 1, six AlGaAs layers in the lower part of the top DBR are composed of high Al-content (98% for the bottom two and and 96% for the remaining four) to form a small oxide aperture for current and optical confinement and a larger oxide aperture (twice the inner aperture diameter) for reducing device capacitance [8]. In a second dry-etching process, the bottom contact layer is reached and the n-contact layers are evaporated. The etched mesas are embedded in a low-k dielectric (BCB) to further reduce the parasitic capacitances [10], [13]. After the

TABLE I
SUMMARY OF DEVICES UNDER TEST

Device	Inner aperture diameter	Surface etch
A	9 μm	0 nm
B	6 μm	55 nm
C	9 μm	55 nm
D	14 μm	55 nm

bondpad sputtering, a shallow surface etch is made in selected VCSELs to optimize top-DBR reflectivity (and consequently the cavity photon lifetime). Table I summarizes the design elements of different VCSELs.

B. Experimental Setup and Measurements

To perform CW measurements, each VCSEL was placed on a copper stage with active temperature control. The emitted optical power was detected by a calibrated, large-area photodiode (UDT Sensors PIN-10D) for accurate measurements. Measurements were performed over an ambient temperature range of 15-100 °C. For spectral measurements, the light was coupled into a multimode fiber connected to an optical spectrum analyzer. All spectral measurements were performed with 0.1 nm resolution. As a result, device temperatures deduced from the spectral data are accurate to within 1.6 °C.

Experimental data from CW measurements is presented in Fig. 2. Part (a) shows the maximum emitted optical power (P_{max}) as a function of T_a. A straight line can be fitted for each case. At T_a corresponding to $P_{max} = 0$, each VCSEL stops lasing. It is important to note that the internal device temperature under such conditions is higher than T_a. Our VCSELs are projected to stop lasing between 128 and 145 °C. This indicates that the cut-off temperature strongly depends on VCSEL cavity design. From this point on, we present measurements and simulations corresponding to $T_a = 55$ °C only. This is a moderately high T_a for which the P_{max} of all the devices exceeds a few milliwatts and device temperatures exceed 120 °C at bias currents corresponding to thermal rollover.

Parts (b)-(d) of Fig. 2 show P_{opt}, V_b and P_{tot} as a function of I_b, respectively, under CW operation at $T_a = 55$ °C. Comparing devices A and C with the same inner aperture diameter (9 μm), as the shallow surface etch in the top DBR is increased from 0 to 55 nm, the transmission-loss rate increases from 0.058 to 0.653 ps^{-1}. As shown in Fig. 2(b), this in turn causes P_{max} and I_b corresponding to P_{max} to increase by 150% and 30% respectively. Electrically, these two devices are identical (a shallow surface etch in the top DBR has an insignificant effect on electrical properties). This leads to almost identical R_s for the two devices over the entire range of I_b, as shown in the inset of Fig. 2(c). Finally, comparing the rate of increase of P_{tot} with I_b for the two devices [Fig. 2(d)], it can be seen that power dissipated as heat in device A exceeds that in device C. In subsequent sections, we will discuss the origin of this excess power dissipation.

Comparing devices B, C, and D, for which inner aperture diameter increases from 6 to 14 μm, both R_{th} and R_s are reduced [18]. This in turn, progressively increases P_{max} and
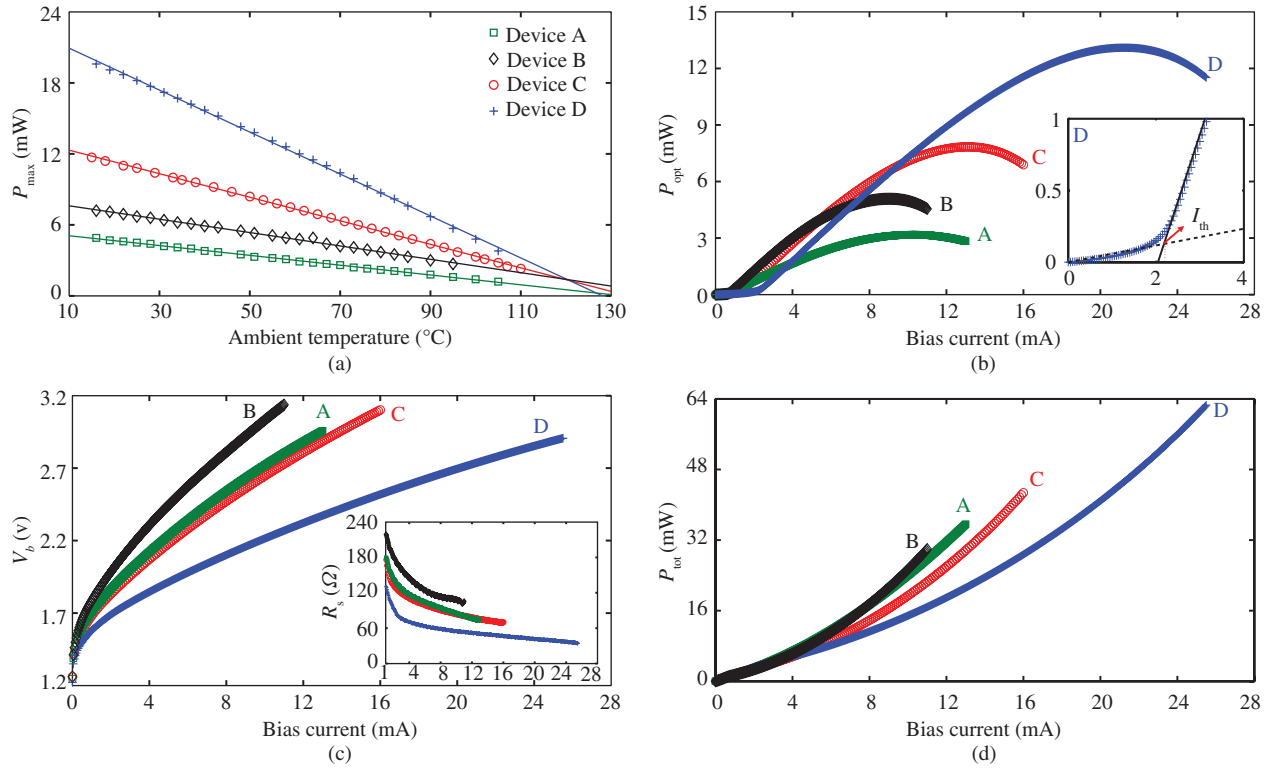
Fig. 2. (a) $P_{\max}$ as a function of T_a for the four VCSELs. (b) P_{opt}. (c) V_b. (d) P_{tot} as a function of I_b at $T_a = 55$ °C. The inset in (b) shows a two-segment line-fit on device D for estimating threshold current and inset in (c) shows the differential resistance R_s.

I_b corresponding to $P_{\max}$, as seen in Fig. 2(b). The series resistance R_s plotted in the inset of Fig. 2(c), is reduced with increasing aperture diameter. As the diameter is increased, the rate of increase of P_{tot} with I_b is reduced [see Fig. 2(d)]. Since the rate of increase of P_{tot} is proportional to rate of increase of device temperature [see Eq. 5], clearly inner aperture diameter strongly influences the VCSEL thermal properties.

Table II summarizes the values of VCSEL parameters at $T_a = 55$ °C deduced from the measurements for the four VCSELs. It also summarizes the errors in the measured values of VCSEL parameters. It is important to understand the sources of errors in the extracted device parameters values. The uncertainty in the value of α_m^T is related to the ±2 nm uncertainty in the surface etch depth. For the analysis presented here, it is ignored [8]. Bias-current-induced increase in device temperature [17] is a prominent source of error in the parameter values. It depends on the ambient temperature T_a owing to the temperature dependence of thermal impedance [see Eq. (5)] and increasing difficulty in stabilizing high stage temperatures against room temperature. At low ambient temperatures, the error in the extracted parameter values corresponds to the resolution limit of the device thermometer which is limited by the resolution of the optical spectrum analyzer [13], [17]. Assuming a worst-case value of 5 °C at $T_a = 100$ °C for all our devices, the corresponding worst-case errors in the parameter values are given in Table II.

Temperature dependencies of internal quantum efficiency and threshold current (I_{th}) were estimated from the measured P_{opt}-I_b curves [18]. I_{th} was calculated using a two-segment

line-fit at any ambient temperature for all the devices. This method is relatively insensitive to changes in slope efficiency [18]. The inset of Fig. 2(b) applies this method to device D for calculating I_{th} at 55 °C ambient temperature. A parabolic fit to measurements at different ambient temperatures is used to model the dependence of I_{th} on device temperature [17]; maximum error in I_{th} is less than 2% for any device. The method for extracting temperature dependence of internal quantum efficiency is described in [17]. A function of the form $\eta_i(T) = \eta_i(RT)/[1 + (T/T_{\mathrm{cr}})^4]$ is used to numerically fit to the measurements; $\eta_i(RT)$, where RT stands for room temperature, can be measured independently [8], [21] and T_{cr} is used as the fitting parameter. The values of T_{cr} are also summarized in Table II. It is important to note that T_{cr} for any device is quite close to $T_{\max}$, the temperature at which the corresponding VCSEL is projected to stop lasing [Fig. 2 (a)]. The maximum calculated error in the extracted value of η_i is less than 1%. Transmission losses through the top and the bottom DBR were calculated numerically using an effective index model [17]. Additional details on the method used to extract temperature dependence of various VCSEL parameters from CW measurements, the origin of errors in their values, physical explanations behind the temperature dependence, and previously reported room temperature values can be found in [8], [13], [17]. Since the dimensional dependence of thermal impedance follows a simple analytical expression [18], $R_{\mathrm{th}} = 1/(2\xi d)$, where ξ is the effective thermal conductivity and d is the inner aperture diameter, we can check the validity of our extraction method

TABLE II
PARAMETER VALUES AT $T_a = 55$ °C FOR THE FOUR VCSELs AND THEIR
LINEAR TEMPERATURE DEPENDENCE ($\triangle = \frac{\partial}{\partial T}$)

| Device	A	B	C	D
λ (nm)	852.7 ± 0.33	853.8 ± 0.33	853.9 ± 0.32	853.8 ± 0.31
R_{th} (°C/mW)	2.07 ± 0.035	2.88 ± 0.03	1.97 ± 0.022	1.27 ± 0.036
α_i (ps^{-1})	$(8.3 \pm 0.22) \times 10^{-2}$	$(8.3 \pm 0.22) \times 10^{-2}$	$(8.3 \pm 0.22) \times 10^{-2}$	$(8.3 \pm 0.22) \times 10^{-2}$
α_m^T (ps^{-1})	0.0578	0.653	0.653	0.653
α_m^B (ps^{-1})	6.08×10^{-3}	6.08×10^{-3}	6.08×10^{-3}	6.08×10^{-3}
$\triangle\lambda$ (nm/°C)	$(6.077 \pm 0.13) \times 10^{-2}$	$(6.198 \pm 0.20) \times 10^{-2}$	$(6.199 \pm 0.14) \times 10^{-2}$	$(6.151 \pm 0.15) \times 10^{-2}$
$\triangle R_{th}$ (mW^{-1})	$(5.4 \pm 0.4) \times 10^{-3}$	$(5.8 \pm 0.2) \times 10^{-3}$	$(3.0 \pm 0.3) \times 10^{-3}$	$(2.0 \pm 0.6) \times 10^{-3}$
$\triangle\alpha_i$ (ps^{-1}/°C)	$(4.167 \pm 0.11) \times 10^{-4}$	$(4.167 \pm 0.11) \times 10^{-4}$	$(4.167 \pm 0.11) \times 10^{-4}$	$(4.167 \pm 0.11) \times 10^{-4}$
$\triangle\alpha_m^T$ (ps^{-1}/°C)	-3.622×10^{-5}	-3.643×10^{-4}	-3.643×10^{-4}	-3.643×10^{-4}
$\triangle\alpha_m^B$ (ps^{-1}/°C)	-5.705×10^{-6}	-5.705×10^{-6}	-5.705×10^{-6}	-5.705×10^{-6}
T_{cr} (°C)	153	154	145	142
T_{max} (°C)	135	133	145	129
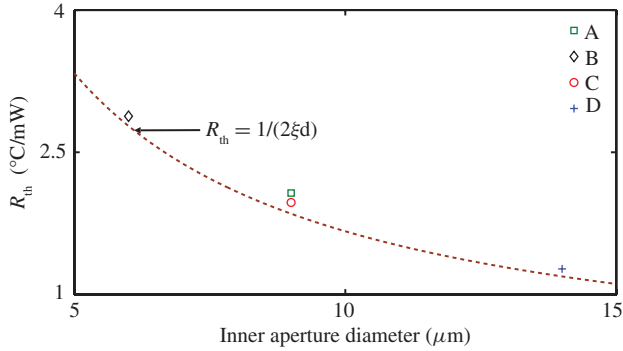
Fig. 3. Thermal impedance as a function of inner aperture diameter. The dashed line represents analytical prediction and symbols correspond to values extracted using our thermal model.

for this particular parameter by comparing its deduced value with the analytical estimate. The expression used to extract R_{th} can be written as [13]

$$R_{th} = \frac{\Delta T}{\Delta P_{tot}} = \frac{\partial\lambda/\partial P_{tot}}{\partial\lambda/\partial T}. \qquad (7)$$

The average values of $\partial\lambda/\partial T$ used are given in Table II. The value of ξ is estimated to be 30 W/(m · K) at 55 °C [18]. Fig. 3 shows an excellent agreement between the analytical result (dashed line) and the our extracted values of thermal impedance.

IV. PREDICTIONS OF OUR THERMAL MODEL

In this section we use the parameter values extracted from CW measurements (see Table II) to study how these parameters influence the thermal rollover mechanisms. We also look at how selected VCSEL parameters evolve with increasing bias current and the influence of this evolution on thermal rollover behavior. We use the procedure outlined in [17], together with the parameters listed in Table II, to simulate the basic VCSEL characteristics. Fig. 4 shows the measured and predicted values of P_{opt}, P_{tot}, and T, respectively, as a function of I_b at $T_a = 55$ °C for the four VCSELs. It can be seen in parts (a) and (b) that the quantitative agreement

is not the same for all devices. However, even for the worst case (Device D), the mismatch is less than 10%. We thus conclude that theoretical predictions based on Eqs. (1), (5), and (6) are in reasonable agreement with the measured data for all devices across the entire range of I_b. This depicts the optical, electrical, and thermal consistency of our thermal model as well as quantifies the underlying accuracy of the derived temperature dependence of VCSEL parameters.

We next consider changes in selected VCSEL parameters with bias current to gain some insight into the origins of thermal rollover. In Fig. 5(a), we plot the variation of η_i and I_{th} with I_b for all four VCSELs. Devices B, C, and D have similar η_i values (about 75 %) at low bias currents, whereas device A has a significantly higher value of 86 %. The physical reason behind this difference will be discussed in the next section. It can be clearly seen that, at high I_b corresponding to the onset of thermal rollover, there is a sharp decrease in the values of η_i and a corresponding increase in the values of threshold current. The rapid decrease in the value of η_i at high device temperatures [Fig. 4 (c)] is responsible for the onset of thermal rollover. Since the emitted optical power is $\propto (I_b - I_{th})$, an increase in the threshold current reinforces the sharp reduction in the value of η_i and hastens the output power saturation. However, the deleterious effect of threshold current can be independently mitigated by optimizing wavelength detuning between the gain peak and the cavity resonance at which the VCSEL operates [22].

Fig. 5(b) depicts how the LPD coefficient K [Eq. (4)] varies with I_b for 4 VCSELs at $T_a = 55$ °C. Close to I_{th}, the value of K is close to 2 W/A but it decreases quite rapidly as the drive current is increased. It takes a minimum value and begins to increase gradually on further increase in I_b. This peculiar evolution is common to all VCSELs and can be understood as follows [17]: Consider first heating due to the carrier recombination which is high below the lasing threshold. This is due to the fact that a significant percentage of the injected carriers recombine spontaneously to produce heat. It is reduced near and beyond the laser threshold because of the clamping of the carrier density. Further, the recombination heating coefficient scales with I_{th}/I_b [17].
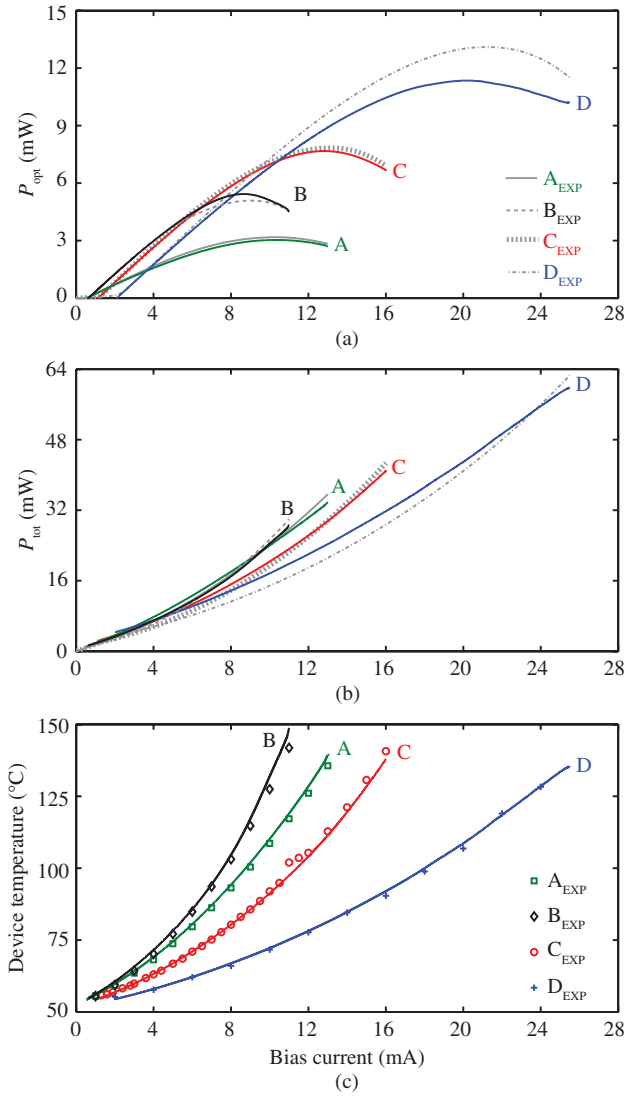
Fig. 4. Comparison of predicted (colored lines) and measured values (indicated by gray lines and symbols) of (a) P_{opt}, (b) P_{tot}, and (c) T as a function of I_b at $T_a = 55$ °C for the four VCSELs.

Fig. 5. (a) Changes in η_i (solid lines) and I_{th} (dashed lines, right scale) with bias current at $T_a = 55$ °C for four VCSELs. (b) LPD coefficient K versus I_b for four VCSELs, inset shows K and P_{opt} for device A as a function of I_b. An increase in K marks the onset of thermal rollover.

Optical absorption (absorption of photons produced by stimulated emission in the VCSEL cavity) starts at the lasing threshold and its contribution increases with I_b due to an increase in the number of stimulated photons. The net effect of carrier recombination and optical absorption is an initial reduction of K with increasing I_b around threshold. It is important to note that carrier thermalization and carrier leakage are low and nearly constant over these low bias currents and hence do not have a significant impact on the evolution of K.

With further increase in I_b, K in Fig. 5(b) takes its relatively low values for all four VCSELs. For these I_b values, carrier thermalization and absorption heating are nearly constant while spontaneous recombination and carrier leakage are slowly decreasing and increasing, respectively. The net effect is a nearly constant K. With a further increase in bias current, increase in carrier leakage dominates, causing an increase of K and a corresponding super-linear increase of P_{LPD}. Further, absorption heating saturates at I_b corresponding to P_{max}, which is consistent with the saturation of the stimulated photon density in the laser cavity.
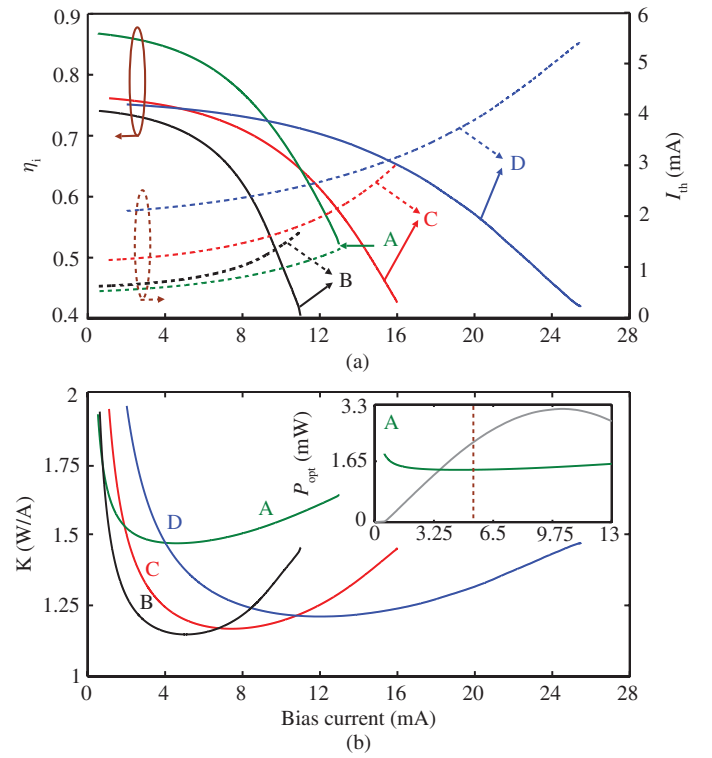
To impress the importance of LPD mechanisms on the thermal performance of these devices, we plot in the inset of Fig. 5(b), P_{opt} and K as a function of I_b for device A at $T_a = 55$ °C. As indicated by the vertical dashed line, as I_b is increased beyond 5.5 mA, the LPD coefficient increases, whereas the emitted optical power begins to saturate. All devices exhibit this behavior. The LPD coefficient therefore, has a profound influence on thermal saturation behavior of all VCSELs. If by some design modification, the onset of increase in LPD coefficient can be delayed, then both the static and dynamic performance can be improved considerably for this class of devices. We turn our attention to this issue in the next section.

V. IMPACT OF DEVICE PARAMETERS

In this section, we study the impact of device parameters on thermal rollover mechanisms [17]. As seen in Table I, devices A and C are used to study the impact of photon lifetime because it is affected by optical losses introduced by a shallow surface etch in the top DBR. Devices B, C, and D have the same surface etch depth (55 nm) and are used to study the impact of inner aperture diameter d.

A. Photon Lifetime

The photon lifetime τ_p of a VCSEL is given by [8]

$$\tau_p = \frac{1}{\alpha_i(T) + \alpha_m^T(T) + \alpha_m^B(T)}. \qquad (8)$$
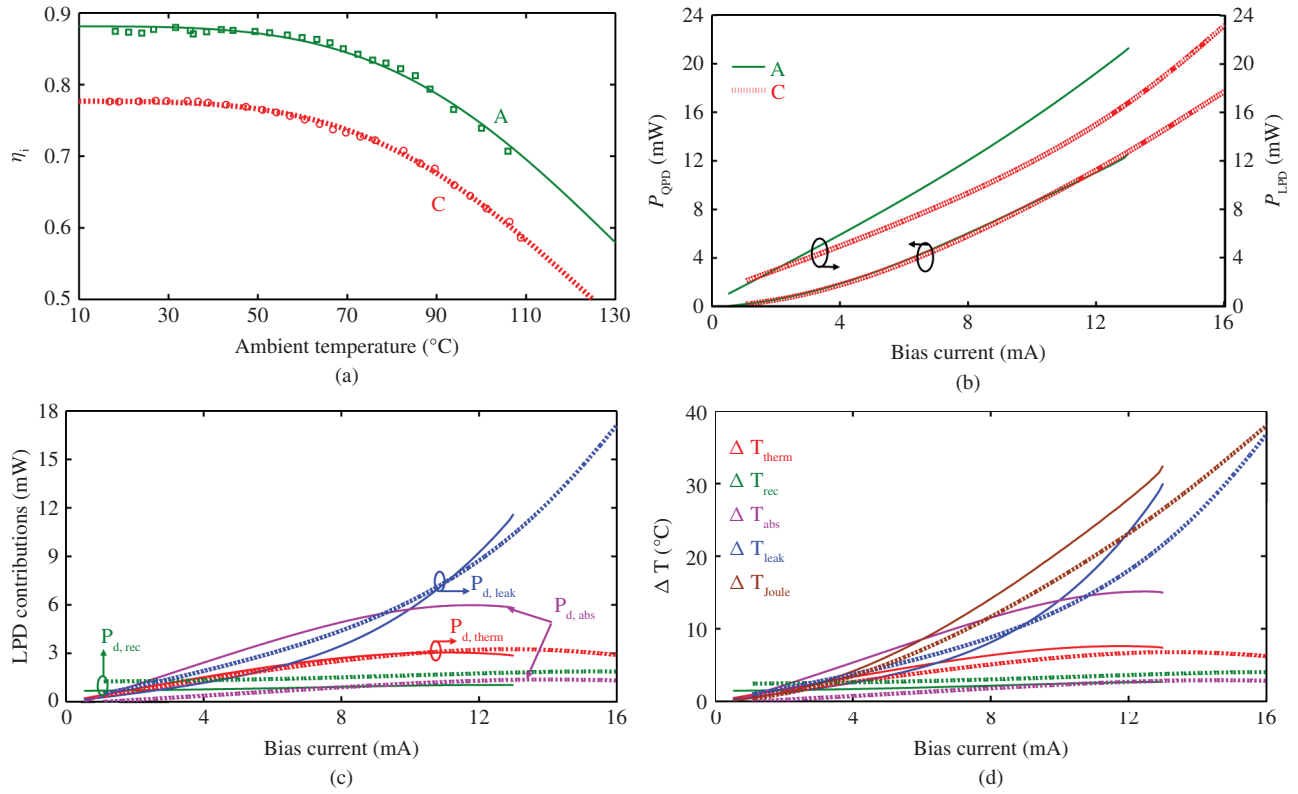
Fig. 6. Impact of photon lifetime on the LPD and QPD mechanisms. (a) Internal quantum efficiency η_i as a function of T_a, solid line show a numerical fit to the data. (b) P_{LPD} and P_{QPD} as a function of I_b. (c) Individual LPD contributions versus I_b. (d) Contributions of LPD and QPD mechanisms to ΔT for device A (solid lines) and device C (dotted lines).

For device A (no surface etch), τ_p is 6.8 ps. This value reduces to near 1.4 ps for devices B, C, and D with the 55-nm surface etch. It has been shown that a shorter photon lifetime improves the high-speed performance of 850-nm VCSELs [8]. Here, we look at the impact of photon lifetime on thermal rollover behavior. For this purpose, it is important to analyze the impact of surface etch on the internal quantum efficiency η_i of a VCSEL. Ideally, a shallow surface etch should not drastically alter η_i. Indeed, the impact on η_i is insignificant for up to a 40-nm surface etch [8]. However, beyond 40 nm, increased cavity losses lead to an increase in the threshold carrier density, which in turn increases carrier leakage, causing a reduction in η_i.

Following our previously reported method for extracting η_i from P_{opt} versus I_b measurements [17], also discussed briefly in section 3, we plot in Fig. 6(a) η_i as a function of T_a for devices A and C. The continuous lines (solid and dotted) correspond to a numerical fit of the data (squares and circles respectively) calculated following the procedure described in Section 3. At any T_a, η_i for device C (with 55-nm etch) is about 10% smaller than that of device A (no etch).

In Fig. 6(b)–(d), solid lines correspond to device A and dotted lines to device C. Fig. 6(b) shows the contributions of P_{LPD} and P_{QPD} to P_{tot} at $T_a = 55$ °C. For both these devices, P_{LPD} exceeds P_{QPD}. This can be attributed to the fact that R_s and K in Eqs. (2) and (3) themselves depend on temperature, and therefore on I_b. As discussed earlier, beyond a certain I_b, while K increases with I_b (Fig. 5b), R_s

decreases with I_b (Fig. 2c). Since similar evolution of K and R_s has been found for all devices, it can be concluded that P_{LPD} is the dominant contributor to the self-heating effects in all four devices. Devices A and C are electrically identical, and therefore the power dissipated across series resistance is identical for both these devices. Since P_{LPD} for device A is significantly higher than that for device C at any I_b, we can conclude that a higher P_{LPD} in device A is limiting its thermal performance.

To understand the reason behind higher P_{LPD} for device A, we plot in Fig. 6(c), the dependence of individual LPD contributions on I_b. It can immediately be seen that P_{abs} is much higher for device A as compared to device C for which P_{abs} is almost negligible. This implies that a surface etch reduces the photon lifetime which not only reduces the damping [8], [18] but also significantly reduces absorption heating which delays the onset of carrier leakage. However, it is important to note that P_{leak} for device C is higher than that for device A at low bias currents.

While a 55-nm-deep surface etch minimizes absorption heating, it does so at the cost of increased carrier leakage at low I_b. On the other hand, the use of a carrier-blocking layer [23] for reducing carrier leakage will increase absorption heating owing to a corresponding increase in the internal quantum efficiency at high bias currents. Therefore, a trade-off exists between absorption heating and carrier leakage in devices that control photon lifetime through a shallow surface etch in the top DBR. This trade-off is different from that

observed in conventional VCSELs involving absorption heating and Joule heating [11], [17]. A general design guideline for this class of devices is that photon lifetime should be optimized to the point where there is an insignificant increase in the threshold carrier density required for lasing. Indeed, devices with a 40-nm surface etch depth have been found to have superior high-speed performance [8]. The residual carrier leakage can then be managed using other techniques such as reducing series resistance [10], thermal impedance [13], and even employing an electron blocking layer [23]. The impact of series resistance and thermal impedance on thermal rollover is discussed later in this section.

Fig. 6(d) shows the contribution of various power dissipation mechanisms to the total heat load. Again, the dominant contribution to increase in device temperature comes from Joule heating and carrier leakage. In device A absorption heating also contributes significantly to the total heat load.

B. Inner Aperture Diameter

Inner aperture diameter (d) is an important VCSEL design parameter from the standpoint of thermal rollover [17]. This is due to the fact that both series resistance ($R_s \propto 1/d^2$) and the device thermal impedance ($R_{th} \propto 1/d$) are reduced with increasing inner aperture diameter [18]. We use devices B, C and D to study the impact of inner aperture diameter on thermal rollover mechanisms.

Fig. 7(a) shows P_{LPD} and P_{QPD} versus I_b at $T_a = 55$ °C for the three devices. The increase in d causes a reduction in R_s at any I_b [Fig. 2(c)], which in turn causes a reduction in P_{QPD}. Comparing the linear power dissipation for these devices, it can be seen that at low I_b, device D has the largest P_{LPD} followed by device C and then device B. However the situation is reversed at high bias currents close to the onset of thermal rollover.

To understand the evolution of P_{LPD} in devices with different d, we plot in Fig. 7(b) the dependence of individual LPD contributions on I_b. Since the three devices have identical surface etch depths, this implies that at low I_b, P_{abs} will be identical for them. Further, the contribution of absorption heating to P_{LPD} is negligible. With increasing I_b, P_{abs} saturates and rolls over. Similar evolution is observed for P_{therm}. For identical surface etch depths, threshold current increases with increasing inner aperture diameter [18]. Above lasing threshold, $P_{rec} \propto I_{th}$ [17]. Since the dominant LPD mechanism at low bias currents is recombination heating for all devices, the device with the largest inner aperture will have the highest P_{LPD} at low bias currents. The situation gets reversed at high bias currents close to the onset of thermal rollover. At those bias currents, with increasing aperture diameter, the onset of increase in carrier leakage is delayed. This in turn delays the onset of thermal rollover [Fig. 4 (a)]. For example, as the inner aperture diameter is increased from 6 to 14 μm, I_b at P_{max} and P_{max} itself both increase by 135% and 160%, respectively. This clearly indicates that VCSELs with a larger inner aperture diameter (≥ 7 μm) exhibit superior CW performance because of a delayed onset of carrier leakage resulting from a reduced series resistance and thermal impedance, which reduces the
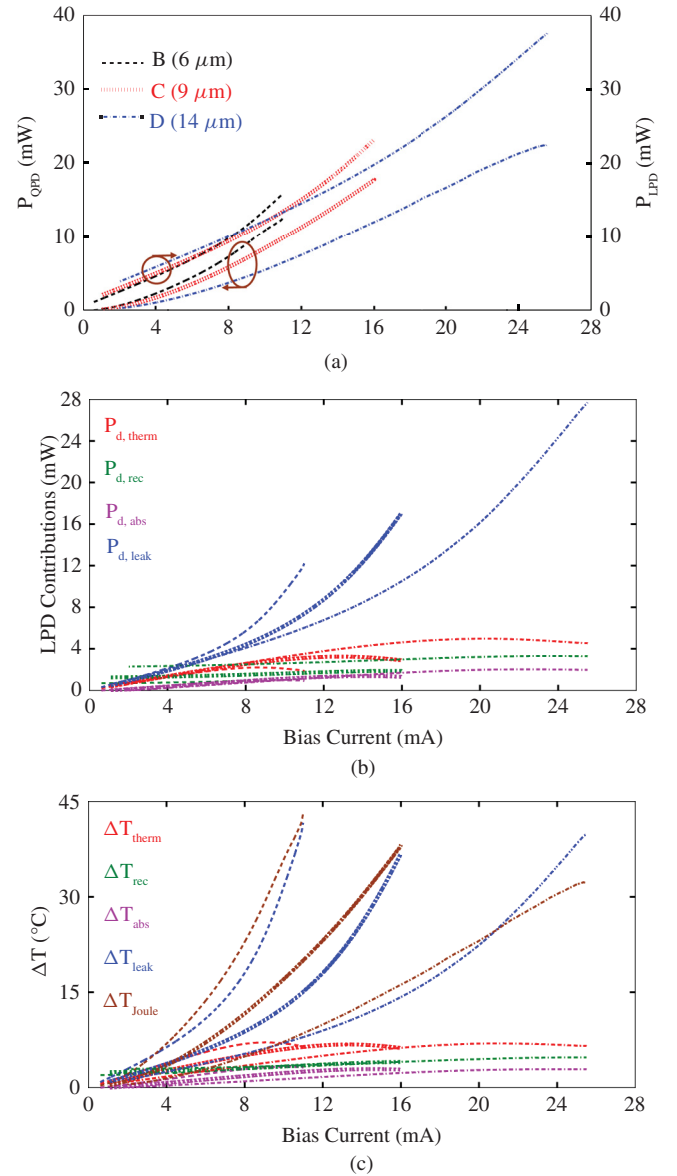

Fig. 7. Impact of inner aperture diameter on the LPD and QPD mechanisms. (a) P_{LPD} and P_{QPD} as a function of I_b. (b) Individual LPD contributions versus I_b. (c) Contributions of LPD and QPD mechanisms to ΔT for device B (dashed lines), device C (dotted lines), and device D (dot-dashed lines).

rate of increase in device temperature with I_b. For the devices investigated in this work, this assertion has been tested for up to 13 μm inner-aperture diameters. However, it is important to understand that an increasing inner-aperture diameter does not translate into superior high-speed performance. As is well known, high-speed performance of a VCSEL is related to the photon density inside its cavity, which decreases with increasing inner-aperture diameters [20].

Fig. 7(c) shows the contributions to increase in the device temperature (ΔT) as a function of I_b at $T_a = 55$ °C. Both P_{QPD} (Joule heating) and P_{leak} dominate the increase in device temperature for all devices and at any I_b. This assertion holds at any ambient temperature [17]. A higher R_{th} for the device with a smaller inner aperture further exacerbates the situation. The device temperatures rapidly increase, reaching rollover

temperatures at lower I_b for smaller-aperture devices. It can therefore be concluded that reducing series resistance and thermal impedance in devices where absorption heating has been reduced can delay the onset of carrier leakage. Reduction in series resistance can be achieved by using intracavity contacts [24] whereas thermal impedance can be reduced by using a binary material in the bottom DBR [13] or by employing metallic heat spreading layers [12].

VI. Conclusion

In this paper, we applied our simple empirical thermal model to study the impact of design parameters on thermal performance of 850-nm VCSELs optimized for high-speed operation. We analyzed four VCSELs, three with different inner aperture diameters (6, 9 and 14 μm) and two with different photon lifetimes (6.8 and 1.4 ps) corresponding to 0 and 55 nm surface etch in the top DBR in devices with 9-μm inner aperture diameter.

Our empirical model requires the temperature dependence of macroscopic VCSEL parameters such as threshold current, internal quantum efficiency, internal optical loss, series resistance and thermal impedance. Adopting a consistent procedure, we deduce the temperature dependence through CW measurements of output power, voltage and emission wavelength as a function of bias current over an ambient temperature range of 15–100 °C. It is important to note that the methods used in this work can potentially be applied to any VCSEL design. As a consequence, aside from some minor modifications in the relations for the barrier bandgap energy, lasing energy, and internal quantum efficiency, our empirical thermal model is generally applicable for a wide class of VCSELs. We demonstrate that our thermal model can reproduce the measured VCSEL characteristics with reasonable accuracy ($< 10\%$ error) for the four VCSELs used in this study, indicating that our model is consistent from the standpoint of optical, electrical, and thermal performance. Such an agreement speaks of the underlying accuracy of the extracted temperature dependence of various VCSEL parameters. A careful analysis of changes in the threshold current and internal quantum efficiency shows that thermal rollover occurs because of a bias-current induced increase in the device temperature which increases the threshold current and causes a sharp reduction in the value of internal quantum efficiency.

The LPD coefficient K [Eq. (4)] shows a similar behavior for all VCSELs. Close to I_{th}, K is quite high because recombination heating dominates in this region. The rapid reduction of K with increasing I_b is due to a reduction in recombination heating coefficient and simultaneous increase in absorption heating coefficient. These two effects reinforce each other. It assumes a minimum value and with further increase in bias current and then begins to increase gradually. This increase in the value of K is singularly dominated by carrier leakage as both absorption and carrier thermalization heating saturate and rollover at these bias currents. We also show that the onset of the optical power saturation coincides with the bias current at which the LPD coefficient K begins to increase. The onset of power saturation in this class of VCSELs can be delayed if the corresponding onset of increase in K is delayed.

An analysis of the evolution of various power dissipation mechanisms with bias current in the four VCSELs yields interesting conclusions. For this entire class of devices, linear power dissipation P_{LPD} exceeds the power dissipated across a series resistance (P_{QPD}). This can be attributed to the fact that, beyond a certain bias current, the proportionality constant for P_{LPD} increases with bias current, whereas the series resistance decreases with bias current. Further, carrier leakage places the ultimate limit on the thermal performance of all these devices.

A comparative thermal analysis of devices A and C, which differ in their cavity photon lifetime, shows a trade-off between absorption heating and carrier leakage. Overcompensating for absorption heating can cause an increase in carrier leakage and vice versa. In these devices, absorption heating is reduced by a shallow surface etch in the top DBR. Beyond a certain etch-depth, cavity losses become so high that a very high carrier density is needed to achieve threshold gain which in-turn increases carrier leakage. Increasing inner aperture diameter reduces the series resistance and thermal impedance. These two effects reinforce each other and this, in turn, delays the onset of carrier leakage, and as consequence a delay in the onset of thermal rollover. While a larger inner-aperture diameter increases the total number of photons inside the cavity, the photon density is actually reduced, resulting in a poorer high-speed performance.

References

[1] R. Dangel, C. Berger, R. Beyeler, L. Dellmann, M. Gmur, R. Hamelin, F. Horst, T. Lamprecht, T. Morf, S. Oggioni, M. Spreafico, and B. J. Offrein, "Polymer-waveguide-based board-level optical interconnect technology for datacom applications," *IEEE Trans. Adv. Packag.*, vol. 31, no. 4, pp. 759–767, Nov. 2008.

[2] J. Tatum, "VCSEL proliferation," *Proc. SPIE*, vol. 6484, no. 1, pp. 648403-1–648403-7, Feb. 2007.

[3] P. Westbergh, J. S. Gustavsson, B. Kógel, A. Haglund, A. Larsson, A. Mutig, A. Nadtochiy, D. Bimberg, and A. Joel, "40 Gbit/s error-free operation of oxide-confined 850 nm VCSEL," *Electron. Lett.* vol. 46, no. 14, pp. 1014–1016, Jul. 2010.

[4] J. A. Kash, A. F. Benner, F. E. Doany, D. M. Kuchta, B. G. Lee, P. K. Pepeljugoski, L. Schares, C. L. Schow, and M. Taubenblatt, "Optical interconnects in future servers," in *Proc. Opt. Fiber Commun. Conf. Exposit. Nat. Fiber Opt. Eng.*, Los Angeles, CA, 2011, pp. 1–3.

[5] J. S. Harris, T. O'Sullivan, T. Sarmiento, M. M. Lee, and S. Vo, "Emerging applications for vertical cavity surface emitting lasers," *Semicond. Sci. Technol.*, vol. 26, no. 1, pp. 014010-1–014010-11, Jan. 2011.

[6] W. Hofmann, P. Moser, P. Wolf, A. Mutig, M. Kroh, and D. Bimberg, "44 Gb/s VCSEL for optical interconnects," in *Proc. Opt. Fiber Commun. Conf. Exposit. Nat. Fiber Opt. Eng*, Los Angeles, CA, 2011, pp. 1–3.

[7] S. B. Healy, E. P. O'Reilly, J. S. Gustavsson, P. Westbergh, A. Haglund, A. Larsson, and A. Joel, "Active region design for high-speed 850-nm VCSELs," *J. Quantum Electron.*, vol. 46, no. 4, pp. 506–512, Apr. 2010.

[8] P. Westbergh, J. S. Gustavsson, B. Kogel, A. Haglund, and A. Larsson, "Impact of photon lifetime on high speed VCSEL performance," *IEEE J. Sel. Topics Quantum Electron.*, vol. PP, no. 99, pp. 1–11, Mar. 2011.

[9] L. F. Lester, S. S. O'Keefe, W. J. Schaff, and L. F. Eastman, "Multiquantum well strained-layer lasers with improved low frequency response and very low damping," *Electron. Lett.*, vol. 28, no. 4, pp. 383–385, Feb. 1992.

[10] Y. Ou, J. S. Gustavsson, P. Westbergh, A. Haglund, A. Larsson, and A. Joel, "Impedance characteristics and parasitic speed limitations of high-speed 850-nm VCSELs," *IEEE Photon. Technol. Lett.*, vol. 21, no. 24, pp. 1840–1842, Dec. 2009.

[11] A. N. Al-Omari and K. L. Lear, "Polyimide-planarized, vertical-cavity surface emitting lasers with 17.0 GHz bandwidth," *IEEE Photon. Technol. Lett.*, vol. 16, no. 4, pp. 969–971, Apr. 2004.

[12] A. N. Al-Omari and K. L. Lear, "VCSELs with a self-aligned contact and copper-plated heatsink," *IEEE Photon. Technol. Lett.*, vol. 17, no. 9, pp. 1767–1769, Sep. 2005.

[13] P. Westbergh, J. S. Gustavsson, A. Haglund, M. Skold, A. Joel, and A. Larsson, "High speed, low-current-density 850 nm VCSELs," *IEEE J. Sel. Topics Quantum Electron.*, vol. 15, no. 3, pp. 694–703, May–Jun. 2009.

[14] W. W. Chow, M. H. Crawford, and R. P. Schneider, "Minimization of threshold current in short wavelength AlGaInP vertical-cavity surface-emitting lasers," *IEEE J. Sel. Topics Quantum Electron.*, vol. 1, no. 2, pp. 649–653, Jun. 1995.

[15] Y.-H. Chang, H.-C. Kuo, F-I. Lai, Y.-A. Chang, C.-Y. Lu, L.-H. Laih, and S.-C. Wang, "Fabrication and characteristics of high-speed oxide-confined VCSELs using InGaAsP-InGaP strain-compensated MQWs," *J. Lightw. Technol.*, vol. 22, no. 12, pp. 2828–2833, Dec. 2004.

[16] J. Shah, "Hot carriers in quasi-2-D polar semiconductors," *IEEE J. Quantum Electron.*, vol. 22, no. 9, pp. 1728–1743, Sep. 1986.

[17] P. P. Baveja, B. Kögel, P. Westbergh, J. S. Gustavsson, A. Haglund, D. N. Maywar, G. P. Agrawal, and A. Larsson, "Assessment of VCSEL thermal rollover mechanisms from measurements and empirical modeling," *Opt. Exp.*, vol. 19, no. 16, pp. 15490–15505, 2011.

[18] L. A. Coldren and S. W. Corzine, *Diode Lasers and Photonic Intergrated Circuits*. New York: Wiley, 1995.

[19] I. Vurgaftman, J. R. Meyer, and L.-R. Ram-Mohan, "Band parameters for III-V compound semiconductors and their alloys," *Appl. Phys. Rev.*, vol. 89, no. 11, pp. 5815–5875, Jun. 2001.

[20] A. Larsson, P. Westbergh, J. Gustavsson, A. Haglund, and B. Kögel, "High-speed VCSELs for short reach communication," *Semicond. Sci. Technol.*, vol. 26, no. 1, pp. 014017-1–014017-5, 2011.

[21] D. V. Kuksenkov, H. Temkin, and S. Swirhun, "Measurement of internal quantum efficiency and losses in vertical cavity surface emitting lasers," *Appl. Phys. Lett.*, vol. 66, no. 14, pp. 1720–1722, Apr. 1995.

[22] C. Wilmsen, H. Temkin, and L. Coldren, *Vertical-Cavity Surface-Emitting Lasers: Design, Fabrication, Characterization, and Applications*. Cambridge, U.K.: Cambridge Univ. Press, 1999.

[23] Y.-A. Chang, T.-S. Ko, J.-R. Chen, F-I. Lai, C.-L. Yu, I.-T. Wu, H.-C. Kuo, Y.-K. Kuo, L.-W. Laih, L.-H. Laih, T.-C. Lu, and S.-C. Wang, "The carrier blocking effect on 850 nm InAlGaAs/AlGaAs vertical-cavity surface-emitting lasers," *Semicond. Sci. Technol.*, vol. 21, no. 10, pp. 1488–1494, 2006.

[24] N. Suzuki, T. Anan, H. Hatakeyama, and M. Tsuji, "Low resistance tunnel junctions with type-II heterostructures," *Appl. Phys. Lett.*, vol. 88, no. 23, pp. 231103-1–231103-3, Jun. 2006.

Petter Westbergh received the M.Sc. and Ph.D. degree in engineering physics and optoelectronics in 2007 and 2011 from the Chalmers University of Technology, Göteborg, Sweden. His current research interests include design, fabrication, and characterization of high-speed 850-nm vertical-cavity surface emitting lasers (VCSELs) and wavelength-tunable VCSELs.

Johan S. Gustavsson received the M.Sc. degree in electrical engineering and the Ph.D. degree in photonics from the Chalmers University of Technology, Göteborg, Sweden, in 1998 and 2003, respectively. He is currently an Assistant Professor in the Photonics Laboratory, Department of Microtechnology and Nanoscience, Chalmers University of Technology. His current research interests include design, modeling, and characterization of long-wavelength semiconductor lasers.

Åsa Haglund received the M.Sc. degree in physics from Göteborg University Göteborg, Sweden, in 2000, and the Ph.D. degree in electrical engineering from the Chalmers University of Technology, Göteborg, in 2005. She is currently an Assistant Professor in the Photonics Laboratory, Chalmers University of Technology. Her current research interests include VCSELs and III-nitride-based light emitters.

Drew N. Maywar received his B.S., M.S, and Ph.D. degrees in optics from the University of Rochesters Institute of Optics in 1993, 1997, and 2000, respectively, and a B.A. in religion from the University of Rochester in 1993. In 2000, Dr. Maywar joined Bell Labs as a Member of Technical Staff. In 2003, he joined the Laboratory for Laser Energetics at the University of Rochester. In 2009, Dr. Maywar joined the Rochester Institute of Technology as assistant professor of telecommunications engineering technology.

Prashant P. Baveja received his B.E. degree from Delhi College of Engineering, University of Delhi, New Delhi, India in 2006. He is currently working towards his Ph.D degree in optics at the Institute of Optics, University of Rochester. His research interests include semiconductor optical amplifiers, vertical cavity surface emitting lasers and optical communications.

Govind P. Agrawal (M'83–SM'86–F'96) Govind P. Agrawal received the M.Sc. and Ph.D. degrees from the Indian Institute of Technology, New Delhi in 1971 and 1974 respectively. After holding positions at the Ecole Polytechnique, France, the City University of New York, and AT&T Bell Laboratories, Murray Hill, NJ, Dr. Agrawal joined in 1989 the faculty of the Institute of Optics at the University of Rochester, where he is a Professor of Optics and Physics, and also a senior scientist at the Laboratory for Laser Energetics.

Benjamin Kögel was born in Herzberg/Harz, Germany, in May 1979. He received the Dipl.-Ing. degree in electrical engineering in 2003 and the Dr.-Ing. degree in 2009, both from the Technische Universität Darmstadt, Darmstadt, Germany. He is currently with the Department of Microtechnology and Nanoscience (MC2), Chalmers University of Technology, Göteborg, Sweden, where he is involved in high-speed and tunable short-wavelength VCSELs.

Anders Larsson received the M.Sc. and Ph.D. degrees in electrical engineering from Chalmers University of Technology, Göteborg, Sweden, in 1982 and 1987, respectively. In 1991, he joined the faculty at Chalmers where he was promoted to Professor in 1994. From 1984 to 1985 he was with the Department of Applied Physics, California Institute of Technology, and from 1988 to 1991 with the Jet Propulsion Laboratory, both at Pasadena, CA, USA. He has been a guest professor at Ulm University (Germany), at the Optical Science Center, University of Arizona, Tucson, Arizona (USA), at Osaka University (Japan), and at the Institute of Semiconductors, Chinese Academy of Sciences (China).